Wind turbine blade trailing edge crack detection based on airfoil aerodynamic noise: An experimental study

Applied Acoustics 191 (2022) 108668

Contents lists available at ScienceDirect

Applied Acoustics

journal homepage: www.elsevier.com/locate/apacoust

Wind turbine blade trailing edge crack detection based on airfoil aerodynamic noise: An experimental study

Yanan Zhang *, Francesco Avallone, Simon Watson

Wind Energy Section, Faculty of Aerospace Engineering, Delft University of Technology, Delft, 2629HS, the Netherlands

ARTICLE INFO

Article history:
Received 22 October 2021
Received in revised form 25 January 2022
Accepted 1 February 2022
Available online 10 February 2022

Keywords:
Wind turbine health condition monitoring
Blade damage detection
Trailing edge crack
Aerodynamic noise

ABSTRACT

In recent years, with the development of the wind power industry and the increase in the number of wind turbines, the condition monitoring of blades and the detection of damage are increasingly important. In this work, a new non-contact damage-detection approach is experimentally investigated based on the measurement of airfoil aerodynamic noise. A NACA 0018 airfoil with chord of 200 mm with different trailing edge crack sizes, 0.2, 0.5, 1.0 and 2.0 mm, is investigated. Experiments are conducted at different mean flow velocities, inflow turbulence intensities and angles of attack. Far-field noise scattered from the airfoil is measured by means of a microphone array. The spectral differences of sound pressure level between the damaged cases and the baseline (without any damage) are compared. As expected, at small angles of attack, with clean or low turbulence intensities (e.g. $\sim$ 4% in the experiment) flow, by increasing the size of the crack, tonal noise appears at trailing-edge thickness-based Strouhal number, St_h, approximatively equal to 0.1. However, at higher angles of attack (e.g. ± 10° and ± 15°) or under conditions of high turbulence intensity (e.g. $\sim$ 7%), the amplitude of the tonal peak diminishes suggesting that complementary measurements or longer acquisition time to remove inflow turbulence effects are needed to monitor trailing edge cracks.

1. Introduction

The decarbonization of the energy system is vital to mitigate the potentially damaging effects of climate change. Wind energy can make a valuable contribution and has seen a huge expansion in recent years [1–4]. For example, in 2020, wind farms in Europe produced 458 TWh, covering 16.4% of electricity demand [5]. Globally, 93 GW of new installed capacity resulted in a 53% growth rate with respect to 2019 [6]. Because of the harsh environment particularly for offshore installations, wind turbines are subject to various types of damage such as structural [7,8], mechanical [9–11] and electrical equipment malfunction [12,13]. Wind turbine blades, amongst other components, are subject to mechanical damage that can affect energy production [14]. A statistical analysis, focusing on failures in Swedish wind farms during 1997–2005, indicated that blade damage represented 13.4% of all failures while gearboxes and generators contributed 9.8% and 5.5%, respectively [15]. Other studies [14,16,17] also report similar conclusions.

The foregoing discussion highlights the need for effective condition monitoring to prevent serious wind turbine blade damage. At present, blade monitoring is performed primarily by visual inspection and regular planned maintenance that require the wind turbines to be shut down. Therefore, the development of real-time non-contact health monitoring techniques is of some interest. Health monitoring techniques can be classified as contact and non-contact. Contact techniques are usually based on vibration [18–21] or strain [22–24] measurements with sensors installed on the blades. Even if direct measurements on the blade guarantee high quality data, information about the damage is reliable only close to the sensor location because of the high damping coefficient of the blades which are made of fiberglass composite material. Furthermore, although sensors can be retrofitted to the blades, this is cumbersome, adds cost, is not always reliable. Ideally, sensors should be embedded in the blade during manufacturing. On the other hand, non-contact approaches rely on measurements acquired with remote systems such as infrared thermography, lasers, microphones, or a combination of these. Infrared thermography can be used for blade damage detection [25,26], but it is limited by its spatial resolution and dynamic range. Another damage detection approach is based on lasers [27–29], but to improve laser measurement performance, a pre-treatment for the target surface is necessary. Acoustic measurements have also the potential to be used; however, until recently, mainly vibro-acoustic approaches

* Corresponding author.
E-mail address: Yanan.Zhang@tudelft.nl (Y. Zhang).

https://doi.org/10.1016/j.apacoust.2022.108668
0003-682X/

have been adopted [30–33]. A few studies in the literature focus on the measurement of audible sound (20 Hz to 20 kHz) using microphones. The first approach [34,35] works by mounting audio speakers inside a wind turbine blade and measuring the sound radiated from the blade to identify damage within the structure (e.g., cracks, edge splits or holes. Another approach [36–39] is based on the use of microphones to detect trends, shifts, or spikes in the sound pressure level within the blade cavity. This approach mainly relies on the measurements of the acoustic pressure responses of the flow-induced noise within the blade cavity. On the other hand, it is potentially possible to use aerodynamic noise generated by the wind turbine blades, also known as airfoil self-noise [40], as a source of information for blades health monitoring [41–44]. In this case, the microphones are located outside the blade and the internal speakers are not needed, thus simplifying the detection method.

In recent years, aerodynamic noise from wind turbines has mainly been investigated because it can limit the installation of onshore wind farms from a noise nuisance perspective [45,46]. As a consequence, the focus has been on its reduction [47,48]. However, in offshore applications, where noise emissions are less of a problem, it is possible to use airfoil self-noise as a source of information for damage detection. As a matter of fact, leading edge erosion or icing will affect boundary layer transition over the blades thus causing a variation of the turbulent boundary layer integral quantities at the trailing edge [49]. There will be a variation of the turbulent boundary layer trailing edge noise and, additional noise will be scattered at the roughness location. These noise sources will alter the broadband component of the noise in the low and high frequency ranges, respectively. Other damage, such as trailing edge delamination and cracks, may result in a thicker trailing edge. When the thickness of the trailing edge is larger than 0.3 times the boundary layer displacement thickness, δ^*, at the trailing edge, vortex shedding appears which results in tonal noise in the far-field spectrum [50–52].

The variation in the far-field spectrum can be an indication of damage. However, in real working conditions, the blade is subject to inflow turbulence with variable length scales. This affects the development of the flow over the blade and introduces an additional source of noise, called leading edge impingement noise [48,53], which can alter the far-field noise spectrum and potentially hide the damage-induced spectral features. While previous publications [41–44] have mainly focused on the development of data-driven methods by means of airfoil self-noise for damage detection, we aim at providing a physics-based interpretation of the results, and we extend the previous studies by including a turbulent inflow. In this regard, trailing edge crack detection is investigated due to the presence of a tonal noise component in the spectrum.

The rest of the paper is organized as follows: In Section 2, the details of the experimental setup are described and the test conditions of the experiment are presented together with the characterization of the turbulent inflow. In Section 3, the results of acoustic measurements are shown and the related physics affecting the acoustic characteristics are discussed. Finally, Section 4 summarizes the main conclusions from the experiments.

2. Experimental setup and test conditions

2.1. Experimental setup

2.1.1. Wind tunnel and test model

The experiment was carried out in the anechoic vertical open-jet tunnel (A-tunnel) of Delft University of Technology. The wind tunnel has a contraction ratio of 15:1 and the rectangular test section outlet is 40 cm × 70 cm. The operating free-stream velocity of the wind tunnel can be up to 45 m/s with turbulence intensity below 0.1% of the free-stream velocity for the entire range of operating velocities. The uniformity of the free-stream velocity distribution across the test section is within 0.5% with respect to velocity at the center of the nozzle [54].

The test model is a NACA 0018 airfoil, which is manufactured from solid aluminum using computer numerical control (CNC) machining (surface roughness: 0.05 mm), with chord length C of 200 mm and span length L of 400 mm (the span-chord ratio $L/C = 2$) as shown in Fig. 1(a). The airfoil model has exchangeable trailing edges to allow the testing of different crack configurations. Since there is no model reported in the literature describing how to model a trailing edge crack of the wind turbine blade, in this research, we make the assumption that when a crack occurs there is only a minor shape change resulting in a thickness increase at the trailing edge. To investigate different damage levels, four changeable trailing edge parts with a rectangle crack are designed. The crack widths W are 0.2, 0.5, 1.0 and 2.0 mm, respectively and the sizes of the crack depth D are based on the crack depth-width ratio, D/W, of 1.5. As a consequence, the thicknesses at the trailing edge, $h = W + h_{Baseline}$($h_{Baseline}$ = 0.76 mm is the trailing edge thickness of the standard NACA 0018 airfoil with the chord length of

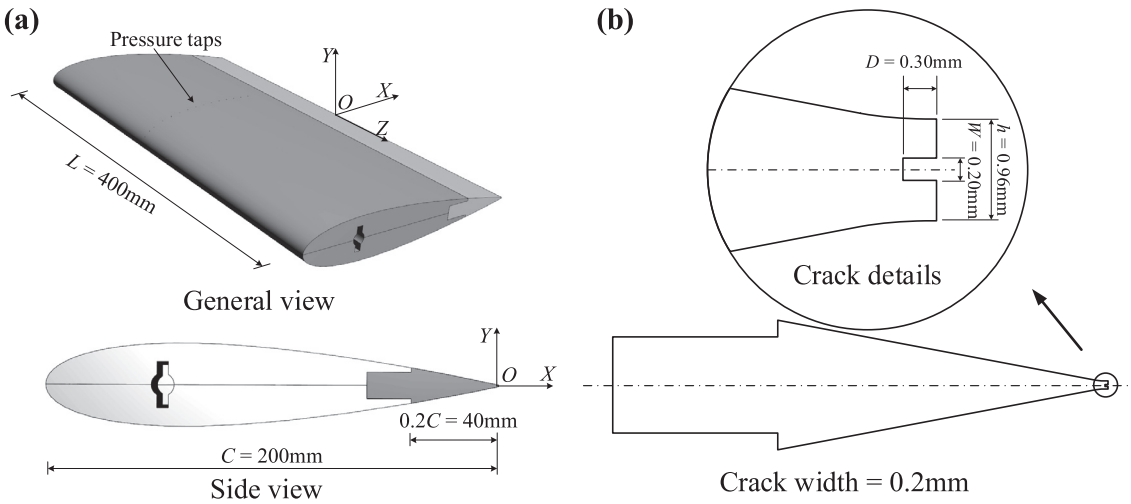

Fig. 1. The test model: (a) NACA 0018 airfoil with baseline trailing edge and (b) an example of the trailing edge with a crack of 0.2 mm.

200 mm), are 0.96, 1.26, 1.76 and 2.76 mm, respectively. The detailed dimensions of the trailing edge parts are shown in Table 1. In Fig. 1(b), an example of the trailing edge with a crack of 0.2 mm is shown. Since the Reynolds numbers at which the experiments were carried out were lower than those likely to be observed in real operating conditions for a full-scale blade, a transition to turbulent flow over the airfoil was forced with two tripping devices located at 20% of the chord at both the pressure and suction side. The tripping device was made of a piece of tape (12 mm width) and sand particles (0.84 mm height) which were distributed randomly with average density of 20 particles per square centimeter. The tested airfoil was installed between two 1.2 m long side plates to guarantee a two-dimensional flow. The leading edge of the airfoil was located at 0.3 m from the nozzle exit. The sketch of the experimental setup is shown in Fig. 2.

For convenience, two coordinate systems (*O-XYZ* and *o-xyz*) are used both taking the geometric center of the trailing edge as an origin. For the *O-XYZ* coordinate system, shown in Fig. 1(a), the *X*-axis is aligned with the chord while, for the *o-xyz* coordinate system, shown in Fig. 2, the *x*-axis is aligned with the direction of the free-stream velocity.

The geometrical angle of attack (AoA) α of the airfoil was set using a stepper motor. The effective AoA α^* of the airfoil is smaller than geometrical angle due to the nature of the flow in an open test section [40]. To obtain the effective AoA, surface pressure measurements were acquired and the results were compared with XFOIL [55]. A total of 15 pressure taps with a diameter of 0.4 mm distributed in the range $-0.99 \leqslant X/C \leqslant -0.34$ at both pressure and suction sides were used for this purpose. The pressure taps are tilted 15° with respect to the centerline to avoid near wake interference from the downstream taps. The pressure taps were connected to pressure transducers with a measurable range of ±2.5 kPa and an accuracy of 12.5 Pa. Pressure data were recorded for a period of 2 s with a sampling frequency of 100 Hz and then averaged. The coefficient of lift C_l at different angles of attack can be obtained by integrating the surface pressure data.

The measured C_l at different values of α is shown in Fig. 3. For comparison, the calculated values of C_l from XFOIL are also shown. By fitting straight lines to these two sets of points, a correction factor can be derived from the ratio of the geometrical to effective angle of attack, $\zeta = \alpha/\alpha^*$, which in this experiment is $\zeta = 0.1130/0.0544 = 2.08$. Unless otherwise specified, for the remainder of this paper, AoA refers to the geometrical angle of attack.

2.1.2. Phased microphone array and beamforming

One single microphone can only measure the overall sound level, which has the limitation of not distinguishing the locations of sound sources. Since in the experiment, the noise sources of the trailing edge are of interest, a microphone array was adopted. The microphone array consists of 64 *G.R.A.S. 40PH* free-field microphones with a frequency response within ±1 dB from 50 Hz to 5 kHz and within ±2 dB from 5 to 20 kHz allowing a maximum output of 135 dB (reference pressure 20 μPa). The microphones were distributed as a 2-D planar array which was parallel to the stream-wise direction. The microphone array was located at 1 m from the airfoil trailing edge as shown in Fig. 2 and the distribution of the microphones in the array is shown in Fig. 4.

The sampling frequency f_s of each microphone was 51.2 kHz and for each test case, the signal was recorded for a length of 20 s. The signal from each microphone was separated into time blocks with 5120 samples ($\Delta t = 100$ ms) for each Fourier transform and spectral average. This provides a frequency resolution of 10 Hz thus making it possible to distinguish the narrowband characteristics of the signal. Furthermore, to avoid energy leakage of the Fourier transform, a Hanning weighting function with 50% data overlap was adopted. Conventional frequency domain beamforming [56,57] was performed on a square grid (scan plane) on the *xoz* plane over an area defined by: $-0.5\text{ m} \leqslant x + x_{Ref} \leqslant 0.5\text{ m}$ and $-0.5\text{ m} \leqslant z + z_{Ref} \leqslant 0.5\text{ m}$ with a space between the grid points of 20 mm where (x_{Ref}, z_{Ref}) is the reference position of the central microphone (solid blue point in Fig. 4). To separate the

Table 1
The dimensions of the trailing edge parts.

Trailing edge No.	0 (Baseline)	1	2	3	4
W (mm)	0	0.20	0.50	1.00	2.00
D (mm)	0	0.30	0.75	1.50	3.00
h (mm)	0.76	0.96	1.26	1.76	2.76
W/C (%)	0	0.10	0.25	0.50	1.00
D/C (%)	0	0.15	0.375	0.75	1.50
h/C (%)	0.38	0.48	0.63	0.88	1.38

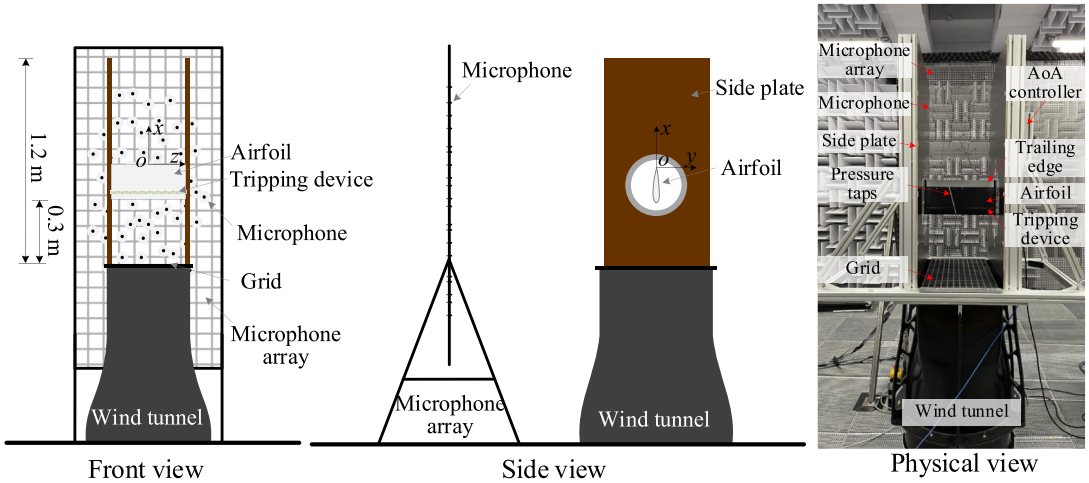

Fig. 2. A sketch of the experimental setup.

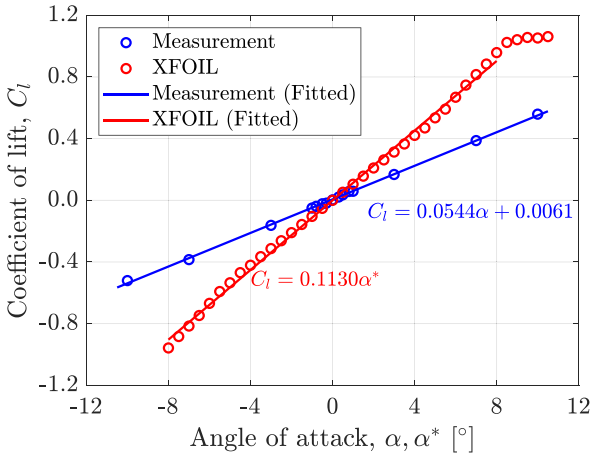

Fig. 3. The relationships between C_l, α and α^* from the measured data and XFOIL.

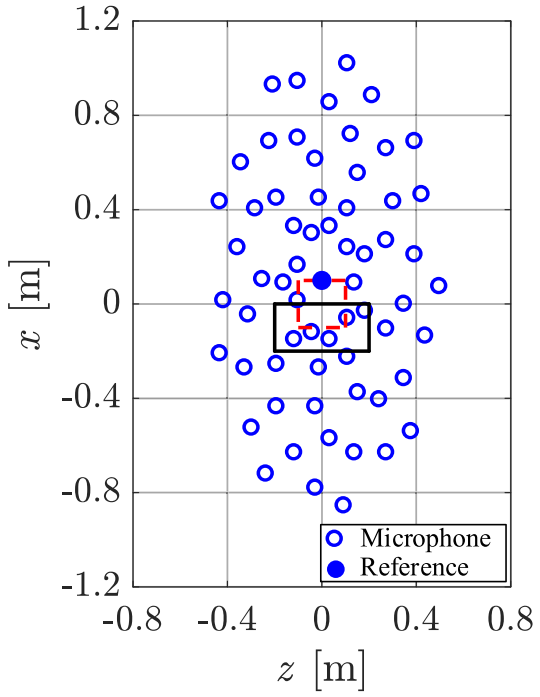

Fig. 4. The distribution of the microphones in the array. The black solid box is the projection of the airfoil onto the array plane with an AoA of 0° and the red dashed box is the corresponding integration region for the sound power. (For interpretation of the references to colour in this figure legend, the reader is referred to the web version of this article.)

trailing edge noise from other undesired sound sources, a region on the scan plane over an area defined by: $-0.1\ \text{m} \leqslant x \leqslant 0.1\ \text{m}$ and $-0.1\ \text{m} \leqslant z \leqslant 0.1\ \text{m}$ was chosen for integration in which all the relevant noise sources from the trailing edge were included [58,59]. The integration region of the sound power and its relative position with respect to the airfoil are shown in Fig. 4.

2.1.3. Turbulence generating grids

As the flow of the wind tunnel is laminar, to simulate the turbulent conditions expected in a realistic operating environment and to further verify the feasibility of the approach under such turbulent conditions, two grids were used for the generation of turbulence [60–63]. Fig. 5 shows the design of the two grids and their geometric dimensions are listed in Table 2. The widths of the two grids are slightly smaller than the space between the two side plates holding the airfoil to avoid side edge noise.

Turbulence downstream of the grid was characterized using hotwire anemometry. Data were sampled at a frequency of 51.2 kHz. The characterization was carried out without the airfoil installed in the test section. To check the uniformity of the turbulence, data were collected at 5 points along the $-x$ direction upstream of the airfoil leading edge and 11 points in the spanwise direction; the spacing between two points was 20 mm, as shown in Fig. 6. For each measurement, data were recorded for 20 s.

Turbulence is characterized through its intensity I and integral length scale Λ_f. The intensity is defined as:

$$I = \frac{u'}{\bar{U}} \tag{1}$$

where $\bar{U}$ is the mean flow velocity and u' is the root-mean-square of the turbulent velocity fluctuations. From the time series, the turbulence integral time scale Λ_t can be calculated from the autocorrelation function,$R_{\tau\tau}(\tau) = \frac{\overline{u(t)u(t+\tau)}}{u^2}$ $(u(t) = U(t) - \bar{U}$, where $U(t)$ is the measured time sequence of the flow velocity and here $\bar{\cdot}$ denotes the time average), and:

$$\Lambda_t = \int_0^\infty R_{\tau\tau}(\tau)\mathrm{d}\tau \tag{2}$$

Then the integral length scale, Λ_f, can be calculated as follows where Taylor's hypothesis of frozen turbulence is applied [64,65]:

$$\Lambda_f = \Lambda_t \bar{U} \tag{3}$$

Also, Eqs. (3) and (4) can be written in the form of an autocorrelation function based on the displacement of the vortex ($R_{xx}(x)$, where $x = \tau \bar{U}$):

$$\Lambda_f = \int_0^\infty R_{xx}(x)\mathrm{d}x \tag{4}$$

2.2. Test conditions

2.2.1. Mean flow velocity

Experiments were performed at five mean flow velocities $\bar{U}$ as reported in Table 3 together with the corresponding chord-based Reynold numbers ($Re_C = \bar{U}C/\nu$, ν- kinematic viscosity).

2.2.2. In-flow turbulence conditions

The power spectral densities (PSDs) of the turbulent fluctuations under different mean flow velocities are shown in Fig. 7. Results show the broadband characteristics of the spectral content. Turbulence intensities of flow without and with the grids under different mean flow velocities are listed in Table 4.

In Fig. 8, the measured autocorrelation for each grid is plotted as a function of displacement from the center of the leading edge together with an exponential fit of the form $R_{xx}(x) = e^{-x/\Lambda_f}$. The resulting turbulence length scale for each grid is given in Table 5.

2.2.3. Angle of attack

A change in AoA of the airfoil leads to a change of the boundary layer properties both at the pressure and suction sides, which can have an effect on far-field noise. In the experiment, seven different values of AoA were tested. Because the microphone array was located on one side of the airfoil, the conditions with non-zero AoA were tested for both positive and negative values. A positive AoA is defined as the trailing edge rotated away from the microphone array. The corresponding effective AoA α^* is determined

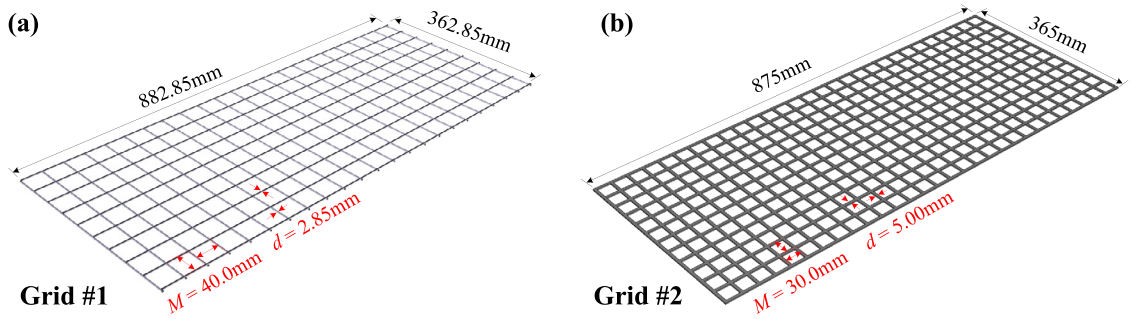

Fig. 5. Turbulence generating grids used in the experiment: (a) #1 and (b) #2.

Table 2
Dimensions of the two turbulence generating grids.

Grid No.	Beam Type	Grid Space, M (mm)	Beam Size, d (mm)	Length (mm)	Width (mm)
#1	Rod	40.0	2.85	882.85	362.85
#2	Flat	30.0	5.00	875	365

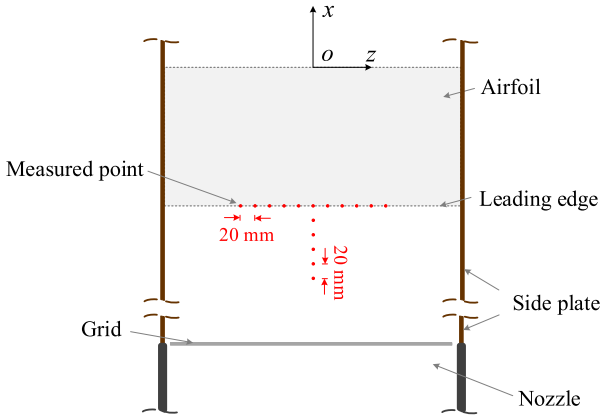

Fig. 6. Turbulence characterization positions.

by the ratio $\zeta = \alpha/\alpha^*$ mentioned in Section 2.1.1. Table 6 shows both the geometrical and effective AoA values.

3. Results and discussion

3.1. Far-field acoustic measurements

The metric generally adopted for acoustic measurement is the sound pressure level (SPL). Integration within a specific bandwidth is also performed, for example, a narrow band (10 Hz, bands of SPL spectra in this work) or one-third octave band (bands of beamforming sound maps in this work), which is defined as:

$$L_p = 10\lg\left(\frac{p^2}{p_{ref}^2}\right) \tag{5}$$

where p' is the root-mean-square of sound pressure fluctuations and p_{ref} is the reference pressure which is 20 μPa for air.

As mentioned in Section 2, a phased microphone array was used for the far-field noise measurement. Fig. 9 shows an example of the beamforming maps for the damaged cases and the baseline (0 mm crack size) with the airfoil at an AoA of 0° and mean flow velocity of 35 m/s (clean inflow condition). The one-third octave center frequency for the beamforming map is selected at 1250 Hz, which is integrated between 1130 Hz and 1410 Hz. The beamforming maps clearly show the sound levels at different locations. In this frequency band, the noise scattered from the trailing edges is predominant. Moreover, when comparing these beamforming maps, there is a decay trend in sound levels at the trailing edge for the baseline and$W$ = 0.2, 0.5, 1.0 mm cases, with respect to the beamforming map for the 2.0 mm width crack.

3.2. Spectral features

The sound power is integrated within a 200 mm × 200 mm region centered at the trailing edge midpoint (black dashed boxes in Fig. 9) and normalized by the total power of a unit monopole source within this region. This is referred to a sound power integration (SPI) technique which gives a total sound level within the given integrated region as mentioned in Section 2.

Fig. 10(a) shows the integrated spectra L_p for the four damaged cases, as well as the baseline, with a frequency resolution of 10 Hz under the clean flow condition with a flow velocity of 35 m/s and AoA of 0°. The case with the 2.0 mm crack shows a significant tonal peak (~3dB) in the L_p spectrum at around 1330 Hz, but for samller crack cases, the peaks are not significant but present as broadband humps. Moreover, with the increase in crack width, the peak or hump shifts to a lower frequency and the amplititue increases, while the broadband contributions in the spectra decrease. This is because for a blunter trailing edge, more coherent vortex structures are shed, thus resulting in a stronger tonal peak [66,67]. Fig. 10(b) shows the corresponding SPL differences compared with the baseline case, i.e., $\Delta L_p = L_p - L_{p,Baseline}$. The ΔL_p spectra provide a simple and direct comparison with the baseline case.

Table 3
Mean flow velocities and Reynold numbers in the experiment.

$\bar{U}$(m/s)	15	20	25	30	35
Re_C	2.0×10^5	2.7×10^5	3.4×10^5	4.1×10^5	4.7×10^5

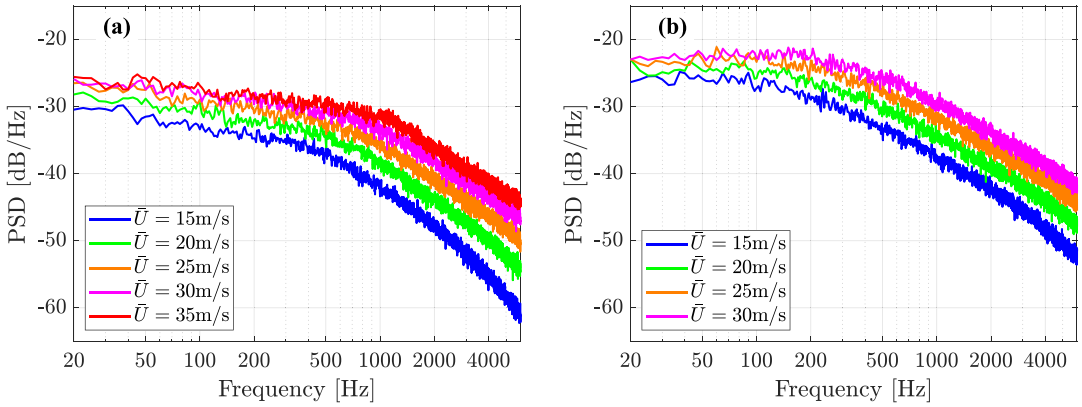

Fig. 7. The spectra of the turbulent flow under different mean flow velocities when the grid is mounted: (a) grid #1 and (b) grid #2.

Table 4
Turbulence intensities (%) of the flow without and with the grids under different mean flow velocity conditions.

$\bar{U}$(m/s)	15	20	25	30	35
No Grid	0.17	0.18	0.18	0.20	0.18
Grid #1	3.71	3.90	4.10	4.21	4.32
Grid #2	6.77	7.03	7.30	7.49	–

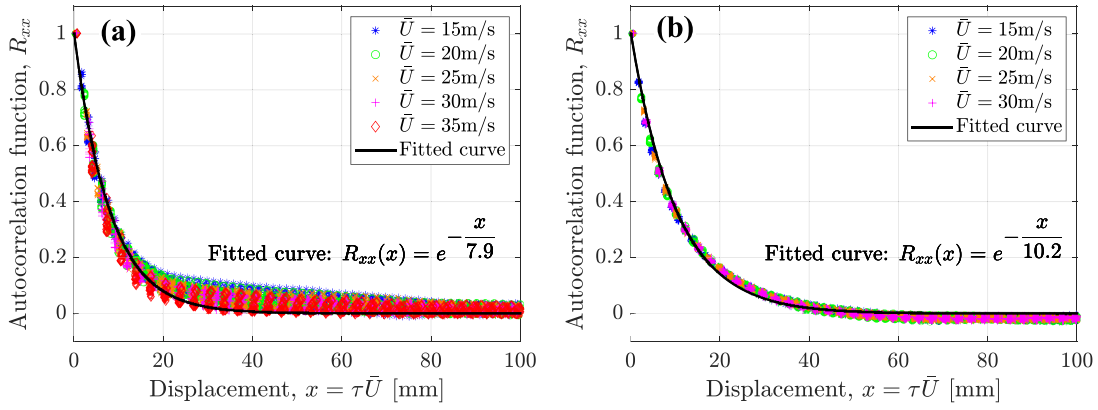

Fig. 8. The autocorrelation function for different mean velocities: (a) grid #1 and (b) grid #2.

Table 5
The turbulence integral length of the flow with the grids.

Grid No.	Turbulence integral length (mm)
#1	7.9
#2	10.2

3.3. Effects of test conditions

3.3.1. Inflow mean flow velocity

In Fig. 11(a), the SPL for the 2.0 mm crack case, with an AoA of 0° and varying laminar inflow velocities is shown. As expected, the SPL increases with increasing free-stream velocity, and as the velocity increases, the spectral peak shifts to the higher frequencies. Fig. 11(b) shows the relationship between the overall sound pressure level (OSPL, integrated from 200 Hz to 8000 Hz) and mean flow velocity. A fit to the points (dashed line) gives an OSPL which varies as a power of 4.82 to the mean flow velocity, which is in line with previous theoretical and numerical research for a sharp trailing edge [40,68,69] where a power of 5 is suggested (solid line in Fig. 11(b)). Fig. 11(c) shows the relationship between the frequency where the sound pressure level peaks (f_{peak}), and the mean flow velocity. A fit to the data shows a linear relationship, which is also found in previous studies [50,70]. This result confirms that the measurements in this study are reliable.

Table 6
The AoA values used in the experiment.

$\alpha(^\circ)$	−15	−10	−5	−3	0	3	5	10	15
$\alpha^*(^\circ)$	−7.21	−4.81	−2.40	−1.44	0	1.44	2.40	4.81	7.21

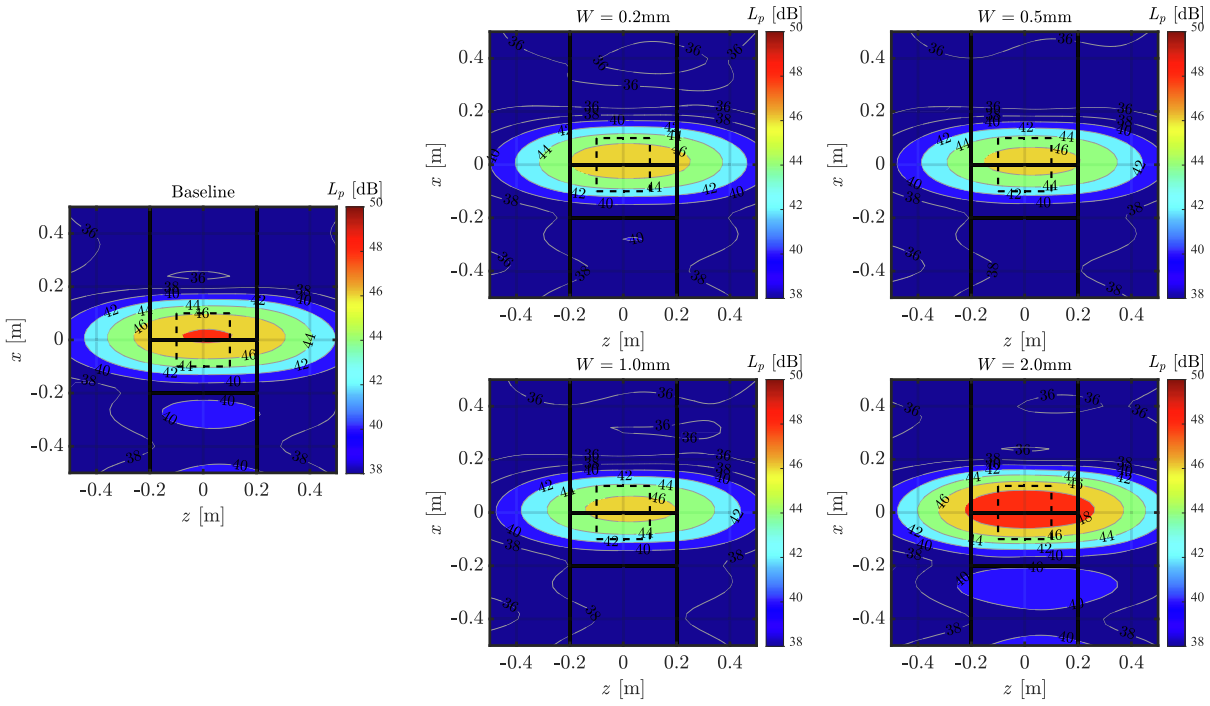

Fig. 9. Beamforming maps of sound pressure level with the one-third octave center frequency of 1250 Hz for the cases with a mean flow velocity of 35 m/s (clean flow condition) and AoA of 0°: the crack widths, W, are 0 (baseline), 0.2, 0.5, 1.0, and 2.0 mm.

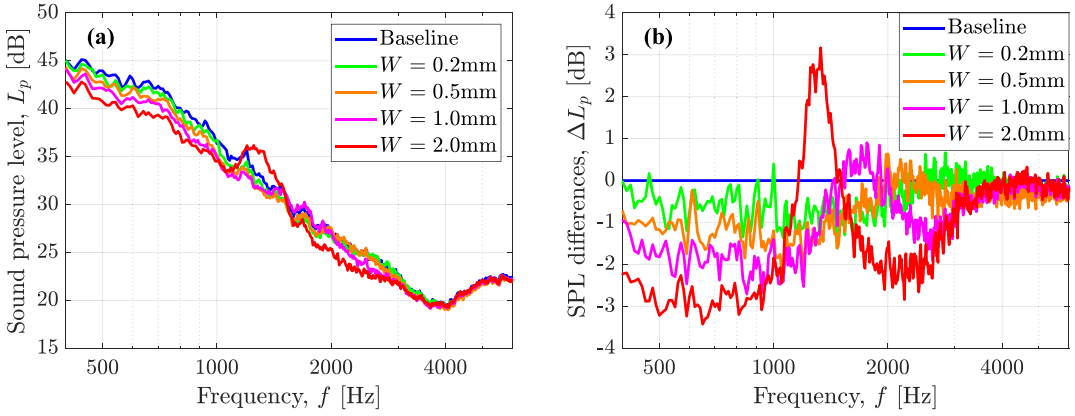

Fig. 10. (a) Spectra of L_p (frequency resolution of 10 Hz) within the integrated region of the case with the mean flow velocity of 35 m/s and AoA of 0°; (b) corresponding spectra of ΔL_p.

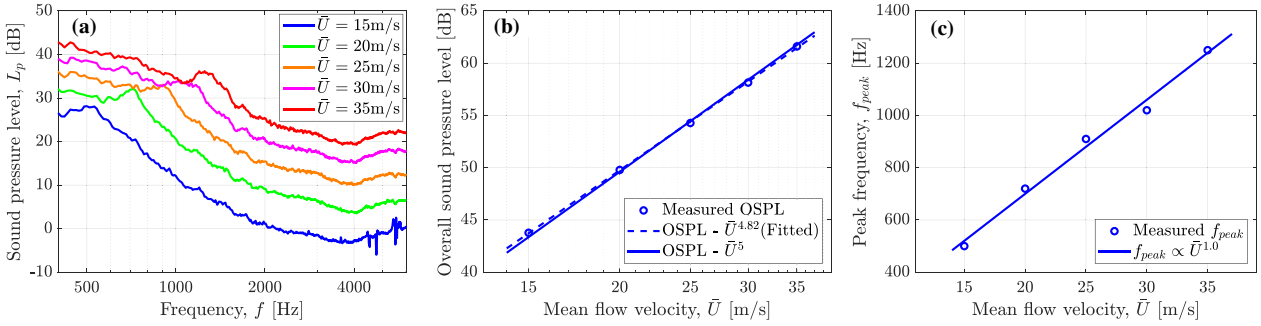

Fig. 11. (a) The SPL of the cases with 2.0 mm crack testing at the AoA of 0° under different mean flow velocities (15, 20, 25, 30, 35 m/s); (b) the relationships between the OSPL and mean flow velocity; (c) corresponding relationships between the frequency of spectral peaks and mean flow velocity.

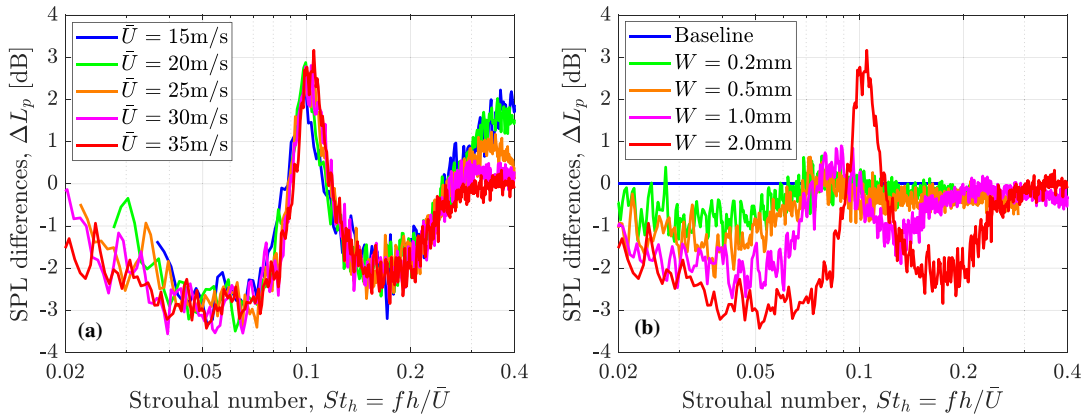

Fig. 12. The relationships between ΔL_p and St_h with AoA of 0°: (a) under different mean flow velocities when crack width is 2.0 mm; and (b) under different crack sizes when mean flow velocity is 35 m/s.

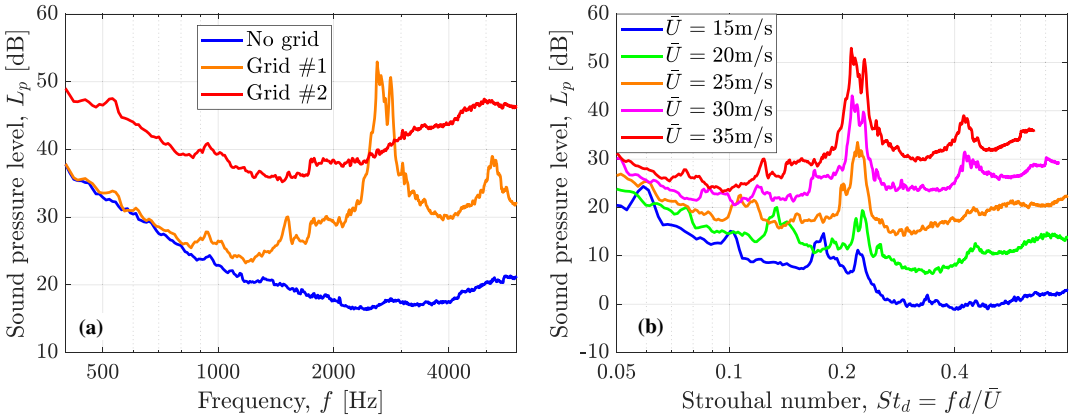

Fig. 13. Spectra of SPL at the integrated region when the airfoil is removed: (a) for a mean flow velocity of 35 m/s and (b) for different mean flow velocities when grid #1 is mounted.

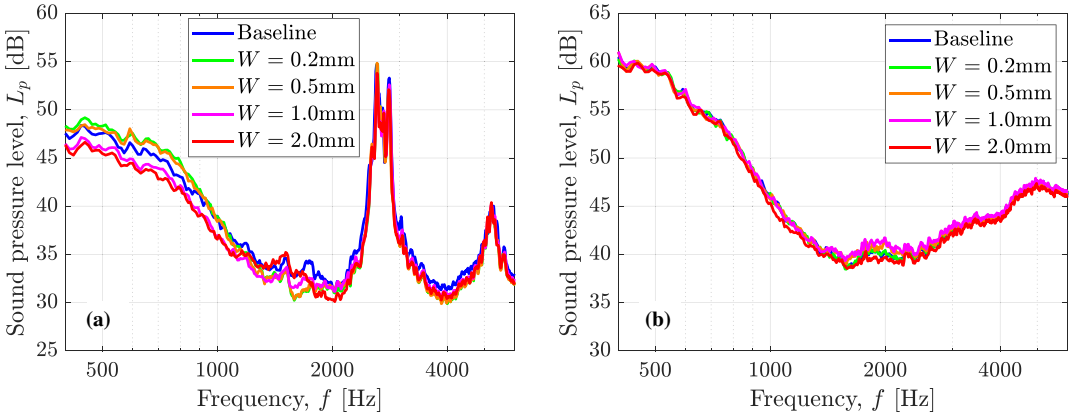

Fig. 14. SPL spectra for different in-flow turbulence conditions when mean flow velocity is 35 m/s and airfoil AoA is 0°: (a) turbulence generated by grid #1 and (b) turbulence generated by grid #2.

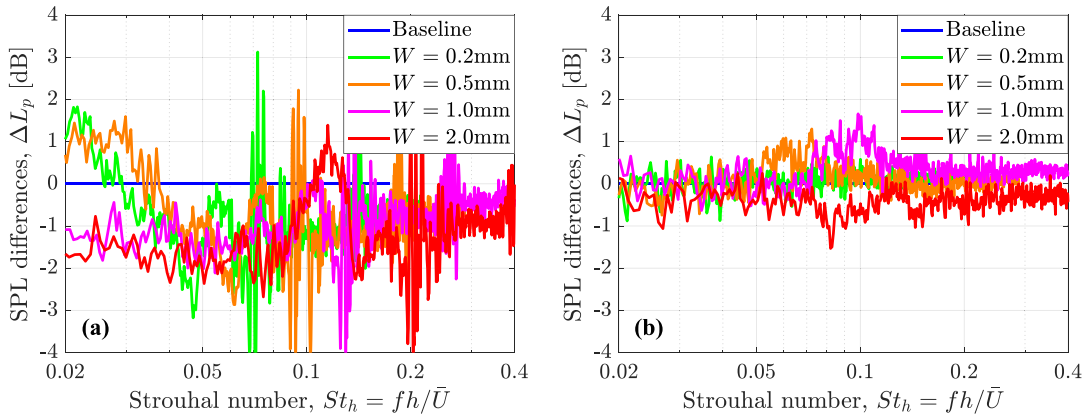

Fig. 15. ΔL_p spectra against St_h for different in-flow turbulence conditions when mean flow velocity is 35 m/s and airfoil AoA is 0°: turbulence generated by grid #1 and (b) turbulence generated by grid #2.

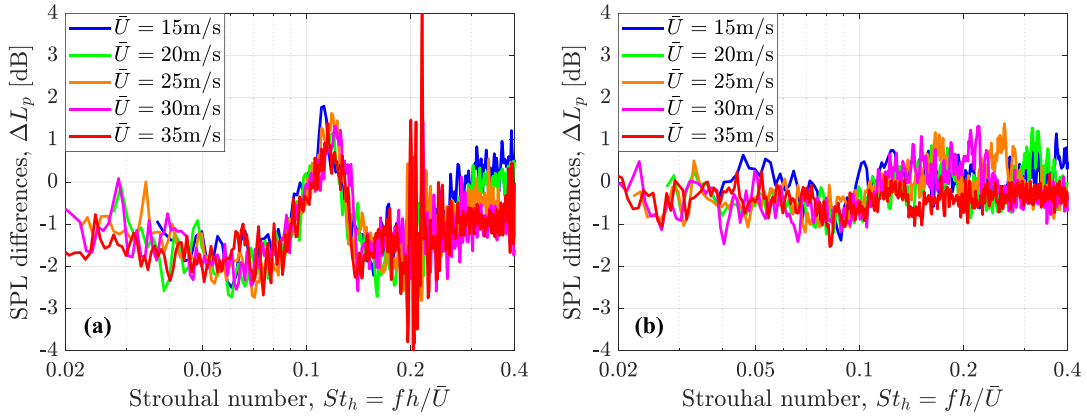

Fig. 16. ΔL_p spectra against St_h for the 2.0 mm crack case for two turbulence conditions: (a) with grid #1 and (b) with grid #2.

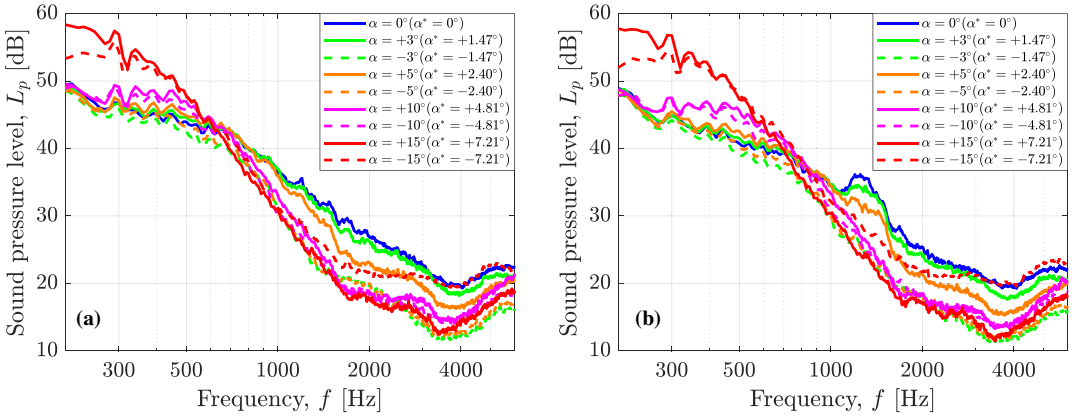

Fig. 17. SPL with a mean flow velocity of 35 m/s at different AoA values when the flow is clean: (a) baseline, (b) crack width of 2.0 mm.

The data are further analyzed as a function of the trailing-edge-thickness-based Strouhal number, $St_h = fh/\bar{U}$, to scale the spectra, as suggested in [40,52,56]. Fig. 12(a) shows ΔL_p as a function of St_h for the 2.0 mm damage case for all flow velocities. All the curves collapse to give a peak at a St_h equal to 0.1 which is in agreement with previous results [40,52,56,71]. The mean flow velocity does not significantly affect the amplitude of this peak. Fig. 12(b) shows ΔL_p as a function of St_h for the different damage cases with AoA equal to 0°. As the crack becomes smaller, the peak broadens and location of the peak shifts to a value of St_h smaller than 0.1.

3.3.2. In-flow turbulence conditions

Fig. 13(a) shows the background noise with the grid installed at a free-stream velocity of 35 m/s. For grid #1, in the lower frequency region, the background noise almost coincides with the no grid case; while at the higher frequencies, there is an increase of the broadband component and the appearance of tonal peaks at 2600 Hz and 5200 Hz. These tones are caused by the grid as demonstrated by the fact that the Strouhal number based on the grid beam diameter $St_d = fd/\bar{U}$ at which they are shed is approximately equal to 0.2 [72], as shown in Fig. 13(b). However, in this experiment, those tonal peaks due to the rod beams of grid #1

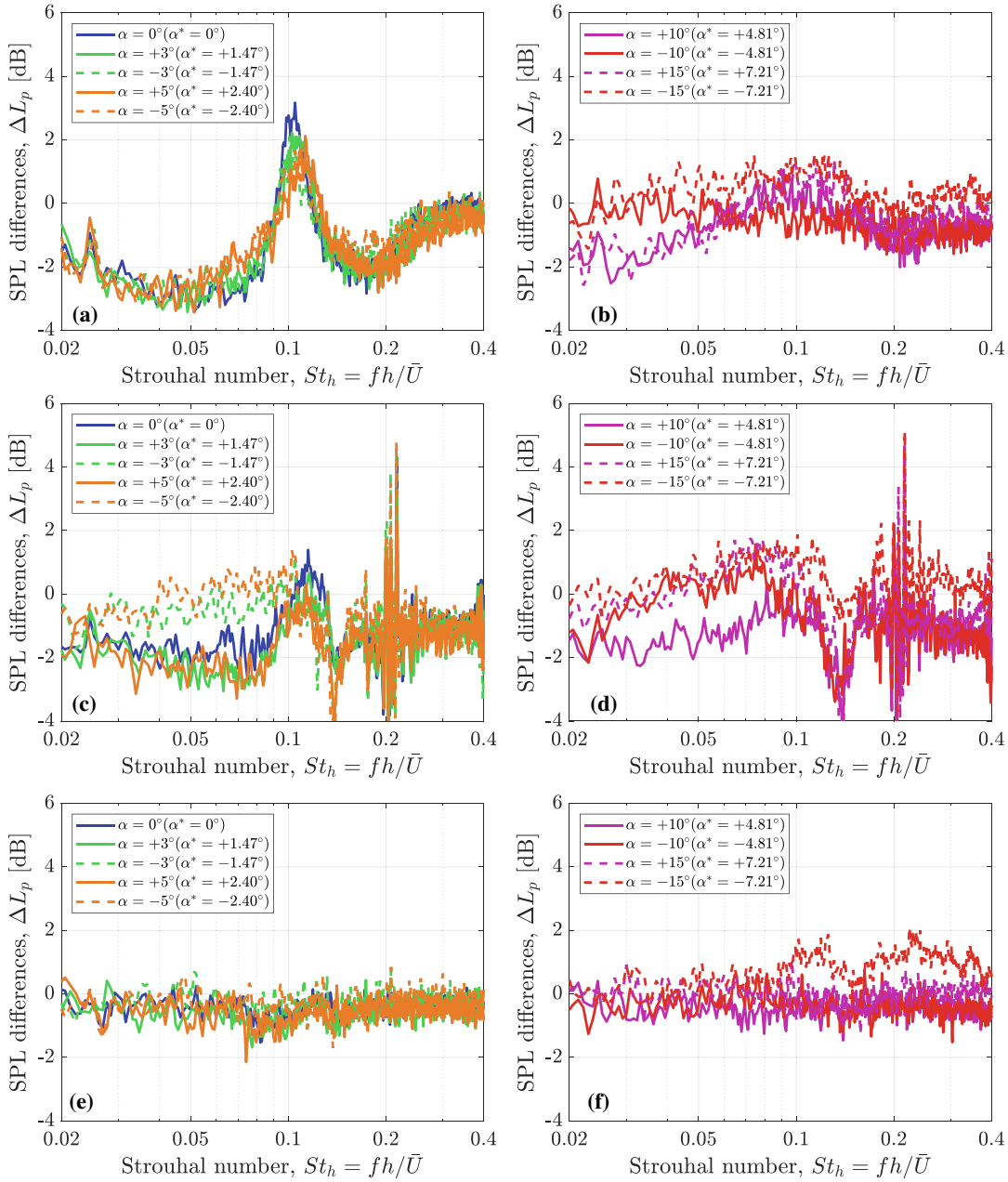

Fig. 18. ΔL_p for the 2.0 mm crack case for different AoA values when mean flow velocity is 35 m/s: (a) no grid, low AoA; (b) no grid, high AoA; (c) grid #1, low AoA; (d) grid #1, high AoA; (e) grid #2, low AoA; and (f) grid #2, high AoA.

are at a higher frequency compared with the characteristic tones related to the blunt trailing edge noise. This means at the low frequency region the data are still reliable. In contrast to grid #1, in Fig. 13(a), grid #2 does not show significant tonal peaks but only broadband background noise.

Fig. 14 shows the sound pressure level spectra for different crack sizes with an AoA of 0° and a mean flow velocity of 35 m/s when grid #1 or grid #2 is mounted. Fig. 15 shows the corresponding spectral differences ΔL_p as a function of St_h. For grid #1, for which the turbulence intensity is $\sim$ 4%, when the crack size is small, i.e., 0.2, 0.5 and 1.0 mm, the spectral differences ΔL_p are not easy to distinguish. When the damage level becomes larger, i.e., 2.0 mm, the spectra of both L_p and ΔL_p show similar trends as the case with clean flow under the same test conditions (shown in Fig. 10(a) and Fig. 12(b)), but with lower amplitude. However, when grid #2 is mounted and the inflow turbulence intensity becomes higher ($\sim$7%), ΔL_p shows very little difference between the different crack cases indicating that the sound characteristics due to the crack (bluntness of trailing edge) cannot be distinguished anymore.

Concerning the sensitivity to the damage when the turbulence condition changes, Fig. 16 shows the spectra of ΔL_p against St_h for the 2.0 mm crack case for these two turbulence conditions. When turbulence is generated by grid #1, the tonal peaks are still distinguishable and the location of the peaks shift slightly to a value of St_h larger than 0.1, while with grid #2, no significant peaks are evident. Compared with the clean flow seen in Fig. 12(a), the amplitude of the tonal peaks clearly diminishes with increasing turbulence intensity.

3.3.3. Airfoil angle of attack

Because of the change in the AoA, the boundary layer both on the pressure and suction side changes; it becomes larger on the suction side and smaller on the pressure side thus affecting vortex formation and its roll-up and, consequently affecting blunt trailing edge vortex shedding noise. Fig. 17 shows the L_p spectra for the baseline and 2.0 mm crack cases at different angles of attack. The mean flow velocity is set at 35 m/s and the inflow is laminar. Since the acoustic array is always at the same position with respect to the test section, the positive AoA is indicated the sound is measured looking at the suction side while the opposite is the case for the negative AoA. For a positive AoA, the spectra of the SPL in the lower frequency range, $f < 600$ Hz, show an increase with increasing AoA, while at the higher frequencies, $f > 600$ Hz, the trend is reversed. This is because the boundary layer is thicker at the suction side increasing the angle of the suction side and there is a redistribution of the energy in the turbulent flow.

Fig. 18(a) and (b) show ΔL_p for the 2.0 mm crack case when the flow is clean for low and high angles of attack, respectively. The peaks caused by the cracks can be found for AoAs up to $\pm 5°$. At higher AoAs, i.e., $\pm 10°$ and $\pm 15°$, the boundary layer on the suction side becomes thicker and the ratio h/δ^* is no longer over the threshold value of 0.3 [50–52], and no tonal peak can be seen. Furthermore, at a higher AoA, the asymmetry between the pressure and suction side may affect the vortex shedding.

The results for turbulent inflow conditions are shown in Fig. 18(c-f). It can be seen that the tonal peak is no longer present for the highest turbulence intensity condition when grid #2 is mounted, thus emphasizing the fact that turbulent inflow conditions might affect the ability to detect cracks from the SPL alone.

4. Conclusions

In this paper, an experimental study focusing on the potential for wind turbine blade trailing edge crack monitoring using airfoil aerodynamic noise was presented. The experimental results showed that it is possible to detect features of the tonal noise caused by the presence of a crack, for clean or low turbulent inflow conditions at moderate angles of attack. As might be expected, larger cracks show more distinct tonal features. However, a turbulent inflow reduces the intensity of the tonal noise caused by the blunt trailing edge. In this work, if the intensity of the turbulent inflow fluctuations is higher than 7% of the free stream velocity, then the blunt trailing edge noise can no longer be detected. By increasing the AoA, the intensity of blunt trailing edge noise decreases and eventually the cracks are no longer detectable.

It can be concluded that it is potentially possible to use airfoil self-noise for trailing edge blade health monitoring, but under certain conditions. It is important to point out that the effect of turbulent inflow could be mitigated by a longer data acquisition time. In addition, a priori knowledge of the boundary layer properties over the airfoil at different radial locations would be required to predict the minimum crack size that can be measured.

Furthermore, the experiments performed have been made under ideal controlled conditions for a stationary airfoil. Clearly, significant further work would be required to assess the efficacy of using acoustic measurements to detect trailing edge cracks on the blades of a full-scale operational turbine in the field.

CRediT authorship contribution statement

Yanan Zhang: Writing – original draft, Conceptualization, Methodology, Data curation, Investigation, Formal analysis, Validation, Software, Visualization, Funding acquisition. **Francesco Avallone:** Writing – review & editing, Methodology, Investigation, Formal analysis, Resources, Supervision. **Simon Watson:** Writing – review & editing, Methodology, Formal analysis, Supervision, Project administration.

Declaration of Competing Interest

The authors declare the following financial interests/personal relationships which may be considered as potential competing interests: Yanan Zhang reports financial support was provided by China Scholarship Council.

Acknowledgements

This work was supported by the China Scholarship Council (CSC) under Grant 201906330095. The authors would like to thank Salil Luesutthiviboon, Dr. Alejandro Rubio Carpio and Dr. Daniele Ragni for their suggestions on experimental design and data processing and Stefan Bernardy for his help with the experimental setup.

References

[1] Enevoldsen P, Jacobson MZ. Data investigation of installed and output power densities of onshore and offshore wind turbines worldwide. Energy Sustain Dev 2021;60:40–51. https://doi.org/10.1016/j.esd.2020.11.004.
[2] deCastro M, Salvador S, Gómez-Gesteira M, Costoya X, Carvalho D, Sanz-Larruga FJ, et al. Europe, China and the United States: Three different approaches to the development of offshore wind energy. Renew Sustain Energy Rev 2019;109:55–70. https://doi.org/10.1016/j.rser.2019.04.025.
[3] Lacal-Arántegui R. Globalization in the wind energy industry: contribution and economic impact of European companies. Renew Energy 2019;134:612–28. https://doi.org/10.1016/j.renene.2018.10.087.
[4] Watson S, Moro A, Reis V, Baniotopoulos C, Barth S, Bartoli G, et al. Future emerging technologies in the wind power sector: a European perspective. Renew Sustain Energy Rev 2019;113:. https://doi.org/10.1016/j.rser.2019.109270109270.
[5] Wind Europe. Wind energy in Europe - 2020 Statistics and the outlook for 2021-2025 2021.
[6] Lee J, Zhao F. Global Wind Report | GWEC. Glob Wind Energy Counc 2021:75.

[7] Ciang CC, Lee JR, Bang HJ. Structural health monitoring for a wind turbine system: a review of damage detection methods. Meas Sci Technol 2008;19. https://doi.org/10.1088/0957-0233/19/12/122001.
[8] Gómez Muñoz CQ, García Marquez FP, Hernandez Crespo B, Makaya K. Structural health monitoring for delamination detection and location in wind turbine blades employing guided waves. Wind Energy 2019;22:698–711. https://doi.org/10.1002/we.2316.
[9] Shanbr S, Elasha F, Elforjani M, Teixeira J. Detection of natural crack in wind turbine gearbox. Renew Energy 2018;118:172–9. https://doi.org/10.1016/j.renene.2017.10.104.
[10] Singh H, Pulikollu RV, Hawkins W, Smith G. Investigation of microstructural alterations in low- and high-speed intermediate-stage wind turbine gearbox bearings. Tribol Lett 2017;65:1–13. https://doi.org/10.1007/s11249-017-0861-5.
[11] Bhardwaj U, Teixeira AP, Soares CG. Reliability prediction of an offshore wind turbine gearbox. Renew Energy 2019;141:693–706. https://doi.org/10.1016/j.renene.2019.03.136.
[12] Alewine K, Chen W. A review of electrical winding failures in wind turbine generators. IEEE Electr Insul Mag 2012;28:8–13. https://doi.org/10.1109/MEI.2012.6232004.
[13] Ibrahim RK, Watson SJ, Djurović S, Crabtree CJ. An effective approach for rotor electrical asymmetry detection in wind turbine DFIGs. IEEE Trans Ind Electron 2018;65:8872–81. https://doi.org/10.1109/TIE.2018.2811373.
[14] Shohag MAS, Hammel EC, Olawale DO, Okoli OI. Damage mitigation techniques in wind turbine blades: a review. Wind Eng 2017;41:185–210. https://doi.org/10.1177/0309524X17706862.
[15] Ribrant J, Bertling L. Survey of failures in wind power systems with focus on Swedish wind power plants during 1997-2005. 2007 IEEE Power Eng Soc Gen Meet PES 2007:1–8. https://doi.org/10.1109/PES.2007.386112.
[16] Dao C, Kazemtabrizi B, Crabtree C. Wind turbine reliability data review and impacts on levelised cost of energy. Wind Energy 2019;22:1848–71. https://doi.org/10.1002/we.2404.
[17] Yang W, Peng Z, Wei K, Tian W. Structural health monitoring of composite wind turbine blades: challenges, issues and potential solutions. IET Renew Power Gener 2017;11:411–6. https://doi.org/10.1049/iet-rpg.2016.0087.
[18] Joshuva A, Sugumaran V. A study of various blade fault conditions on a wind turbine using vibration signals through histogram features. J Eng Sci Technol 2018;13:102–21.
[19] Abdulraheem KF, Al-Kindi G. A Simplified wind turbine blade crack identification using Experimental Modal Analysis (EMA). Int J Renew Energy Res 2017;7:715–22.
[20] Sarrafi A, Mao Z, Niezrecki C, Poozesh P. Vibration-based damage detection in wind turbine blades using Phase-based Motion Estimation and motion magnification. J Sound Vib 2018;421:300–18. https://doi.org/10.1016/j.jsv.2018.01.050.
[21] Oliveira G, Magalhães F, Cunha Á, Caetano E. Vibration-based damage detection in a wind turbine using 1 year of data. Struct Control Heal Monit 2018;25:1–22. https://doi.org/10.1002/stc.2238.
[22] Schroeder K, Ecke W, Apitz J, Lembke E, Lenschow G. A fibre Bragg grating sensor system monitors operational load in a wind turbine rotor blade. Meas Sci Technol 2006;17:1167–72. https://doi.org/10.1088/0957-0233/17/5/S39.
[23] Verbruggen T. Load monitoring for wind turbines. Wind Energy: Fibre optic sensing and data processing; 2013.
[24] Sierra-Pérez J, Torres-Arredondo MA, Güemes A. Damage and nonlinearities detection in wind turbine blades based on strain field pattern recognition. FBGs, OBR and strain gauges comparison. Compos Struct 2016;135:156–66. https://doi.org/10.1016/j.compstruct.2015.08.137.
[25] Yang R, He Y, Mandelis A, Wang N, Wu X, Huang S. Induction infrared thermography and thermal-wave-radar analysis for imaging inspection and diagnosis of blade composites. IEEE Trans Ind Informatics 2018;14:5637–47. https://doi.org/10.1109/TII.2018.2834462.
[26] Manohar A, Tippmann J, Lanza di Scalea F. Localization of defects in wind turbine blades and defect depth estimation using infrared thermography. Sensors Smart Struct Technol Civil Mech Aerosp Syst 2012;2012 (8345):83451O. https://doi.org/10.1117/12.915256.
[27] Talbot J, Wang Q, Brady N, Holden R. Offshore wind turbine blades measurement using Coherent Laser Radar. Meas J Int Meas Confed 2016;79:53–65. https://doi.org/10.1016/j.measurement.2015.10.030.
[28] Hwang S, An YK, Sohn H. Continuous-wave line laser thermography for monitoring of rotating wind turbine blades. Struct Heal Monit 2019;18:1010–21. https://doi.org/10.1177/1475921718771709.
[29] Park B, Sohn H, Malinowski P, Ostachowicz W. Delamination localization in wind turbine blades based on adaptive time-of-flight analysis of noncontact laser ultrasonic signals. Nondestruct Test Eval 2017;32:1–20. https://doi.org/10.1080/10589759.2015.1130828.
[30] Joosse PA, Blanch MJ, Dutton AG, Kouroussis DA, Philippidis TP, Vionis PS. Acoustic emission monitoring of small wind turbine blades. J Sol Energy Eng Trans ASME 2002;124:446–54. https://doi.org/10.1115/1.1509769.
[31] Tang J, Soua S, Mares C, Gan TH. An experimental study of acoustic emission methodology for in service condition monitoring of wind turbine blades. Renew Energy 2016;99:170–9. https://doi.org/10.1016/j.renene.2016.06.048.
[32] Han BH, Yoon DJ, Huh YH, Lee YS. Damage assessment of wind turbine blade under static loading test using acoustic emission. J Intell Mater Syst Struct 2014;25:621–30. https://doi.org/10.1177/1045389X13508329.
[33] Shahidan S, Pulin R, Muhamad Bunnori N, Holford KM. Damage classification in reinforced concrete beam by acoustic emission signal analysis. Constr Build Mater 2013;45:78–86. https://doi.org/10.1016/j.conbuildmat.2013.03.095.
[34] Aizawa K, Poozesh P, Niezrecki C, Baqersad J, Inalpolat M, Heilmann G. An acoustic-array based structural health monitoring technique for wind turbine blades. Struct Heal Monit Insp Adv Mater Aerospace Civ Infrastruct 2015;2015 (9437):94371P. https://doi.org/10.1117/12.2084276.
[35] Poozesh P, Aizawa K, Niezrecki C, Baqersad J, Inalpolat M, Heilmann G. Structural health monitoring of wind turbine blades using acoustic microphone array. Struct Heal Monit 2017;16:471–85. https://doi.org/10.1177/1475921716676871.
[36] Traylor C, DiPaola M, Willis DJ, Inalpolat M. A computational investigation of airfoil aeroacoustics for structural health monitoring of wind turbine blades. Wind Energy 2020;23:795–809. https://doi.org/10.1002/we.2459.
[37] Solimine J, Niezrecki C, Inalpolat M. An experimental investigation into passive acoustic damage detection for structural health monitoring of wind turbine blades. Struct Heal Monit 2020;19:1711–25. https://doi.org/10.1177/1475921719895588.
[38] Beale C, Niezrecki C, Inalpolat M. An adaptive wavelet packet denoising algorithm for enhanced active acoustic damage detection from wind turbine blades. Mech Syst Signal Process 2020;142:. https://doi.org/10.1016/j.ymssp.2020.106754106754.
[39] Beale C, Willis DJ, Niezrecki C, Inalpolat M. Passive acoustic damage detection of structural cavities using flow-induced acoustic excitations. Struct Heal Monit 2020;19:751–64. https://doi.org/10.1177/1475921719860389.
[40] Brooks TF, Pope DS, Marcolini MA. Airfoil self-noise and prediction. vol. 1218. National Aeronautics and Space Administration; 1989.
[41] Fazenda BM, Comboni D. Acoustic condition monitoring of wind turbines: Tip faults. 9th Int Conf Cond Monit Mach Fail Prev Technol 2012, C 2012 MFPT 2012 2012;1:109–23. https://doi.org/10.1121/1.4755203.
[42] Chen B, Yu S, Yu Y, Zhou Y. Acoustical damage detection of wind turbine blade using the improved incremental support vector data description. Renew Energy 2020;156:548–57. https://doi.org/10.1016/j.renene.2020.04.096.
[43] Zhang CQ, Gao ZY, Chen YY, Dai YJ, Wang JW, Zhang LR, et al. Locating and tracking sound sources on a horizontal axis wind turbine using a compact microphone array based on beamforming. Appl Acoust 2019;146:295–309. https://doi.org/10.1016/j.apacoust.2018.10.006.
[44] Tu TH, Lo FC, Liao CC, Chung CF, Chen RC. Using wind turbine noise to inspect blade damage through portable device. INTER-NOISE 2019 MADRID - 48th Int Congr Exhib Noise Control Eng 2019:1–5.
[45] Pawlaczyk-ŁUszczyńska M, Dudarewicz A, Zaborowski K, Zamojska-Daniszewska M, Waszkowska M. Evaluation of annoyance from the wind turbine noise: a pilot study. Int J Occup Med Environ Health 2014;27:364–88. https://doi.org/10.2478/s13382-014-0252-1.
[46] Michaud DS, Feder K, Keith SE, Voicescu SA, Marro L, Than J, et al. Exposure to wind turbine noise: perceptual responses and reported health effects. J Acoust Soc Am 2016;139:1443–54. https://doi.org/10.1121/1.4942391.
[47] Luesutthiviboon S, Ragni D, Avallone F, Snellen M. An alternative permeable topology design space for trailing-edge noise attenuation. Int J Aeroacoustics 2021. https://doi.org/10.1177/1475472X211003295.
[48] Teruna C, Avallone F, Casalino D, Ragni D. Numerical investigation of leading edge noise reduction on a rod-airfoil configuration using porous materials and serrations. J Sound Vib 2021;494:1–25. https://doi.org/10.1016/j.jsv.2020.115880.
[49] Ye Q, Avallone F, Ragni D, Choudhari M, Casalino D. Effect of surface roughness geometry on boundary-layer transition and far-field noise. AIAA J 2021:1–13. https://doi.org/10.2514/1.j059335.
[50] Hasheminejad SM, Chong TP, Lacagnina G, Joseph P, Kim J-H, Choi K-S, et al. On the manipulation of flow and acoustic fields of a blunt trailing edge aerofoil by serrated leading edges. J Acoust Soc Am 2020;147:3932–47. https://doi.org/10.1121/10.0001377.
[51] Blake WK. Mechanics of flow-induced sound and vibration, Volume 2: Complex flow-structure interactions. Academic press 2017.
[52] Oerlemans S. Wind turbine noise : primary noise sources 2011:1–57.
[53] Bampanis G, Roger M, Ragni D, Avallone F, Teruna C. Airfoil-turbulence interaction noise source identification and reduction by leading-edge serrations. 25th AIAA/CEAS Aeroacoustics Conf 2019 2019:1–18. https://doi.org/10.2514/6.2019-2741.
[54] Merino-Martínez R, Rubio Carpio A, Lima Pereira LT, van Herk S, Avallone F, Ragni D, et al. Aeroacoustic design and characterization of the 3D-printed, open-jet, anechoic wind tunnel of Delft University of Technology. Appl Acoust 2020;170. https://doi.org/10.1016/j.apacoust.2020.107504.
[55] Drela M. XFOIL: An analysis and design system for low Reynolds number airfoils. Low Reynolds number Aerodyn., Springer; 1989, p. 1–12.
[56] Oerlemans S. Detection of aeroacoustic sound sources on aircraft and wind turbines 2009:1–173.
[57] Sijtsma P. Phased Array Beamforming Applied to Wind Tunnel and Fly-Over Tests. SAE Tech Pap 2010;2010-Octob:17–9. https://doi.org/10.4271/2010-36-0514.
[58] Merino-Martínez R, Sijtsma P, Carpio AR, Zamponi R, Luesutthiviboon S, Malgoezar AMN, et al. Integration methods for distributed sound sources. Int J Aeroacoust 2019;18:444–69. https://doi.org/10.1177/1475472X19852945.
[59] Sijtsma P, Snellen M. Inverse integration method for distributed sound sources. BeBeC 2018:9–17.

[60] Comte-Bellot G, Corrsin S. The use of a contraction to improve the isotropy of grid-generated turbulence. J Fluid Mech 1966;25:657–82. https://doi.org/10.1017/S0022112066000338.
[61] Groth J, Johansson AV. Turbulence reduction by screens. J Fluid Mech 1988;197:139–55. https://doi.org/10.1017/S0022112088003209.
[62] Kurian T, Fransson JHM. Grid-generated turbulence revisited. Fluid Dyn Res 2009;41. https://doi.org/10.1088/0169-5983/41/2/021403.
[63] Isaza JC, Salazar R, Warhaft Z. On grid-generated turbulence in the near- and far field regions. J Fluid Mech 2014;753:402–26. https://doi.org/10.1017/jfm.2014.375.
[64] Geng C, He G, Wang Y, Xu C, Lozano-Durán A, Wallace JM. Taylor's hypothesis in turbulent channel flow considered using a transport equation analysis. Phys Fluids 2015;27. https://doi.org/10.1063/1.4908070.
[65] Mazellier N, Vassilicos JC. Turbulence without Richardson-Kolmogorov cascade. Phys Fluids 2010;22:1–25. https://doi.org/10.1063/1.3453708.
[66] Thomareisa N, Papadakis G. Effect of trailing edge shape on the separated flow characteristics around an airfoil at low reynolds number: a numerical study. Phys Fluids 2017;29. https://doi.org/10.1063/1.4973811.
[67] Metzinger CN, Chow R, Baker JP, Cooperman AM, Van Dam CP. Experimental and computational investigation of blunt trailing-edge airfoils with splitter plates. AIAA J 2018;56:3229–39. https://doi.org/10.2514/1.J056098.
[68] Oerlemans S, Sijtsma P, Méndez LB. Location and quantification of noise sources on a wind turbine. J Sound Vib 2007;299:869–83. https://doi.org/10.1016/j.jsv.2006.07.032.
[69] Cheng B, Han Y, Brentner KS, Palacios J, Morris PJ, Hanson D, et al. Surface roughness effect on rotor broadband noise. Int J Aeroacoust 2018;17:438–66. https://doi.org/10.1177/1475472X18778278.
[70] Wolf WR, Azevedo JLF, Lele SK. Effects of mean flow convection, quadrupole sources and vortex shedding on airfoil overall sound pressure level. J Sound Vib 2013;332:6905–12. https://doi.org/10.1016/j.jsv.2013.08.029.
[71] Zhu WJ, Shen WZ, Sørensen JN, Leloudas G. Improvement of airfoil trailing edge bluntness noise model. Adv Mech Eng 2016;8:1–12. https://doi.org/10.1177/1687814016629343.
[72] Hutcheson F, Brooks T. Noise radiation from single and multiple rod configurations. Int J Aeroacoust 2012;11:291–334. https://doi.org/10.1260/1475-472X.11.3-4.291.